PHYSICAL REVIEW A VOLUME 22, NUMBER 2 AUGUST 1980

Atomic inner-shell level energies determined by absorption spectrometry with synchrotron radiation

Marianne Breinig,* Mau Hsiung Chen, Gene E. Ice,† Fernando Parente,‡ and Bernd Crasemann
Department of Physics, University of Oregon, Eugene, Oregon 97403

George S. Brown
Stanford Synchrotron Radiation Laboratory, Stanford, California 94305
(Received 2 January 1980)

Absolute energies of the ArK, KrK, and XeL_1, L_2, and L_3 levels have been determined from absorption edges measured with synchrotron radiation. The double-crystal x-ray monochromator was calibrated by a method that ties the energy scale directly to the crystal lattice constant and hc. Theoretical model spectra were constructed from ≥ 4 Lorentzians representing the lowest-energy one-electron electric-dipole transitions to bound excited states, and an arc tangent representing transitions to higher bound states and to the continuum. The transition energies were found by minimizing χ^2 for the fit of the theoretical spectrum shape to the data. Energy differences from optical spectral series were used to relate the excited-state energies to the vacuum level. Results are compared with earlier measurements and with theory.

I. INTRODUCTION

The need for accurate data on the binding energies of inner-shell electrons in neutral atoms has recently become more pronounced.[1] Relativistic self-consistent-field calculations have been carried out, including the effects of relaxation and quantum-electrodynamic (QED) shifts.[2-4] Comparison of the theoretical results with precise experimental level energies can thus provide tests of the QED corrections and of underlying models of atomic structure. Limitations of the independent-particle approximation, in particular, are of interest; through shifts of a few electron volts, the effects of electron-electron Coulomb correlation can appear even in the innermost orbitals of high-Z atoms.

The widely used tables of x-ray atomic energy levels by Bearden and Burr[5] generally fall short of the required accuracy. In this and similar compilations,[6,7] it is not always clear whether the data are derived from free atoms or from solids; in the latter case, extra-atomic relaxation can cause substantial shifts.[8-10] Most often, hybrid approaches have been employed, including optical data for valence orbitals measured on free atoms in gaseous sources, while x-ray data from solids are used for core levels. Combining both to obtain inner-shell binding energies leads to the most common type of systematic error in these tabulations. Large discrepancies exist even among tabulated binding energies of core electrons in noble gases[5,11] (Sec. III D). While level-energy *differences* can be determined from x-ray emission spectrometry with high accuracy,[12] tying these energies to the vacuum (or Fermi) level presents considerable difficulties. Comparisons[2,13,14] of measured and computed atomic level energies have brought out the need for reevaluation and new measurements.[14]

In this paper, we report on determinations of the ArK, KrK, and XeL_1, L_2, and L_3 energy levels from absorption edges measured with synchrotron radiation. High intensity, narrow bandwidth, and tunability of the radiation make it possible to obtain high-resolution spectra with a signal-to-noise ratio of $> 10^3$.[15,16] The monochromator was calibrated absolutely to < 0.1 eV. A theoretical model of the edges was used in a computer fit of the measured spectra to determine energy-level differences; these were related to the vacuum level by matching the energies of excited bound states with terms in corresponding spectroscopic series.

II. EXPERIMENTAL

A. Apparatus

Hard synchrotron radiated from ~3-GeV electrons circulating in the Stanford Positron-Electron Accelerator Ring (SPEAR) was extracted in the Stanford Synchrotron Radiation Laboratory. A narrow x-ray energy band was selected by means of a Bragg-diffraction monochromator that contains two Si crystals in the parallel $(n, -n)$ position (Fig. 1).[17] A stepping motor under computer control causes the crystals to rotate about a common axis, with 4000 or 16 000 steps per degree, respectively, in each of two instruments employed. The parallel-crystal arrangement is capable of high resolution because of the small divergence of the synchrotron-light beam; with a ~1-mm source height at ~20 m from the monochromator, a band-

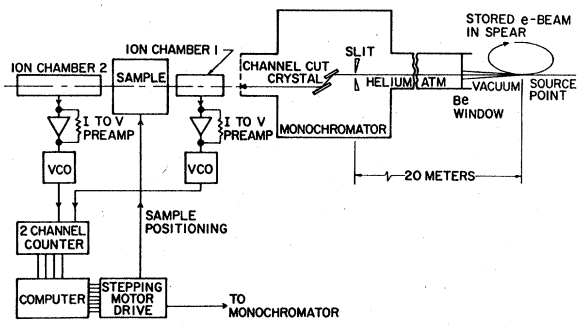

FIG. 1. Block diagram of absorption spectrometer and associated apparatus.

width of ~0.5 eV at 5.4 keV is attained from two Si (220) reflections.

The x-ray beam issuing from the two-crystal monochromators is parallel to the incident beam and displaced vertically by $\Delta h = 2D\cos\theta$, where θ is the Bragg angle and D is the spacing between the crystal faces (~1 cm). A simple tracking system can thus maintain the sample position with respect to the beam.

The monochromatized x rays traverse an ion chamber, the sample-gas cell (made of glass with 0.025-cm-thick Be windows), and a second, longer ion chamber. The charge collected on the plates of each ion chamber produces a current in the nanoampere range that is converted to voltage in Keithley 427 electrometers. The voltage signals drive two voltage-controlled oscillators whose output frequencies are measured by a dual-channel gated scaler interfaced with a PDP-11 computer. The contents of the scalers I_0 and I and their ratio I_0/I are stored by the computer on a floppy disk; at intervals this information is transferred to magnetic tape for further analysis.

The response of the two ion chambers varies differently with photon energy, because they have different lengths and, in some runs, contain different counting-gas mixtures. The chamber efficiencies, however, vary slowly with photon energy. Over a typical edge scan that covers 10 eV, the ratio I_0/I varies smoothly by $< 2\%$ in the absence of a sample. This gradual change in base line does not impair analysis of the absorption spectra. An advantage of the double-ion-chamber method is inherent noise cancellation: Any amplitude fluctuations in the incident photon beam affect both chambers and cancel out in the ratio I_0/I.

B. Application of Bragg's law

The Si crystals in the x-ray monochromator diffract photons of energy E according to Bragg's law,

$$2d\sin\theta = nhc/E \ . \tag{1}$$

Here, d is the spacing between diffracting atomic planes in the crystals; the Bragg angle θ is the angle between the incident ray and the diffracting planes, n is the order of diffraction, h is Planck's constant, and c is the velocity of light. In the application of Eq. (1), corrections must be made for x-ray refraction at the crystal surfaces and for changes in the spacing d caused by thermal expansion.

X rays entering and leaving the crystals are refracted. This phenomenon can be taken into account by replacing the interplanar spacing d in Eq. (1) with an effective spacing

$$d_n = d\left(1 - \frac{4d^2}{n^2}\frac{\delta}{\lambda^2}\right) , \tag{2}$$

where λ is the x-ray wavelength. The quantity δ is the unit decrement of the refractive index μ. The Bragg angles θ_{out} (outside the crystals) and θ_{in} (inside the crystals) are related by

$$\frac{\cos\theta_{\text{out}}}{\cos\theta_{\text{in}}} = \frac{\lambda_{\text{out}}}{\lambda_{\text{in}}} = \mu = 1 - \delta \ . \tag{3}$$

For x-ray energies well removed from absorption edges of atoms in the crystals, i.e., if anomalous scattering and dispersion can be neglected, the classical expression holds for δ:

$$\delta = \frac{e^2\lambda^2}{2\pi mc^2} Nf(0) \ , \tag{4}$$

where N is the number of atoms per unit volume, e and m are the charge and mass of the electron, respectively, and $f(0)$ is the atomic form factor for radiation scattered in the forward direction. To the extent that Eq. (4) holds, the ratio δ/λ^2 is independent of λ and the effective spacing d_n does not depend on the wavelength but only on the order of the Bragg reflection. For Si crystals, Henins and Bearden[18] measured $\delta = (7.6 \pm 0.1)\times 10^{-6}$ for Cu$K\alpha_1$ radiation, i.e., with an uncertainty of 4×10^{-8} Å^{-2} in δ/λ^2 at $\lambda = 1.54$ Å. We take $\delta/\lambda^2 = (3.22 \pm 0.10)\times 10^{-6}$ Å^{-2}, with the uncertainty increased to compensate for the assumption that δ/λ^2 remains constant over the wavelength range $0.8 \leq \lambda \leq 4$ Å.

The lattice parameter a_0, which determines the interplanar spacings d, is the length of the cube side of the conventional unit cell of the diamond structure. For a nearly perfect single crystal of Si, Deslattes and Henins[19] found $a_0 = 5.43106275$ Å at 25 °C and atmospheric pressure, with an uncertainty of only 0.15 ppm. Thermal expansion of the crystal is taken into account by applying the relation

$$a_0(t+\Delta t) = a_0(t)(1+\alpha_{Si}\Delta t) , \quad (5)$$

where t is the temperature. The thermal coefficient of Si crystals[20] is $\alpha_{Si} = (2.56 \pm 0.03)\times 10^{-6}\ K^{-1}$.

C. Monochromator calibration

The geometry of the two-crystal spectrometer is described in terms of the angles and unit vectors indicated in Fig. 2. The monochromator axis is taken to be perpendicular to the x-y plane. The vector $\hat{\vec{n}}_1$ denotes the normal to the surface of the first crystal (C_1), and $\hat{\vec{n}}_2$ denotes the normal to the surface of the second crystal (C_2). The projection of $\hat{\vec{n}}_1$ onto the x-y plane defines the y direction. The vectors $\hat{\vec{n}}_1$ and $\hat{\vec{n}}_2$ lie above the x-y plane at angles δ_1 and δ_2, respectively. The vectors $\hat{\vec{r}}_1$ and $\hat{\vec{r}}_2$ indicate the direction of reference rays incident on C_1 and C_2, respectively. The vector $\hat{\vec{r}}_1$ lies below the x-y plane at an angle ψ. Its projection onto the x-y plane makes an angle η with the x axis. For a perfectly aligned system, the angles δ_1, δ_2, and ψ are zero. We assume that these angles are always small compared with η.

The sine of the Bragg angle for the first crystal is

$$\sin\theta' = -\hat{\vec{r}}_1 \circ \hat{\vec{n}}_1 = \cos\psi \sin\eta \cos\delta_1 + \sin\psi \sin\delta_1 . \quad (6)$$

We set

$$\theta' = \eta + \epsilon_1 \quad (7)$$

($\epsilon_1 \ll 1$), and use the approximation

$$\sin\theta' = \sin\eta + \epsilon_1 \cos\eta . \quad (8)$$

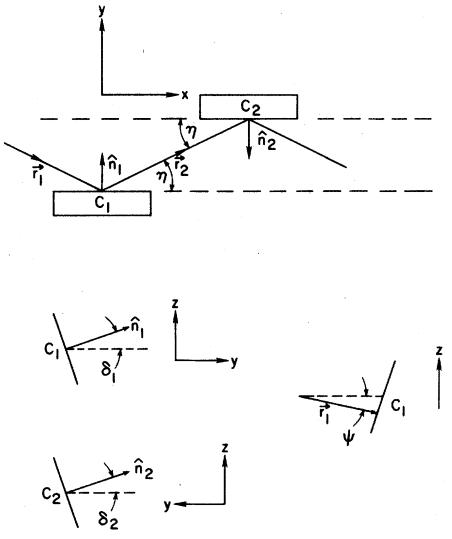

FIG. 2. Angles and unit vectors for the description of the two-crystal spectrometer geometry.

Then we find

$$\epsilon_1 = \frac{(\cos\psi\cos\delta_1 - 1)\sin\eta + \sin\psi\sin\delta_1}{\cos\eta} . \quad (9)$$

To second order in the small angles ψ and δ_1, we have

$$\epsilon_1 = -\tfrac{1}{2}(\psi^2 + \delta_1^2)\tan\eta + \psi\delta_1/\cos\eta . \quad (10)$$

The sine of the Bragg angle for the second crystal is

$$\begin{aligned}\sin\theta'' &= -\hat{\vec{r}}_2 \circ \hat{\vec{n}}_2 \\ &= \cos\psi\cos 2\delta_1 \cos\delta_2 \sin\eta + \sin\psi \sin 2\delta_1 \cos\delta_2 \\ &\quad - \cos\psi \sin 2\delta_1 \sin\delta_2 \sin\eta \\ &\quad + \sin\psi \cos 2\delta_1 \sin\delta_2 . \end{aligned} \quad (11)$$

We set

$$\theta'' = \eta + \epsilon_2 , \quad (12)$$

with $\epsilon_2 \ll 1$. Using the same approximations as in the case of the first crystal, we find

$$\begin{aligned}\epsilon_2 &= -\tfrac{1}{2}(\psi^2 + \delta_1^2)\tan\eta \\ &\quad + (1/\cos\eta)(-2\delta_1 \sin\eta + 2\psi\delta_1 - 2\delta_1\delta_2 \sin\eta + \psi\delta_2) . \end{aligned} \quad (13)$$

If the two crystal faces are perfectly parallel, we have

$$\delta_1 = \delta_2 \quad (14)$$

and

$$\epsilon_2 = -\tfrac{1}{2}(\psi^2 + \delta_1^2)\tan\eta + \psi\delta_1/\cos\eta . \quad (15)$$

In this case of perfect parallelism, ϵ_1 equals ϵ_2, and the angles between the reference ray and the surfaces of C_1 and C_2 are equal. We define one Bragg angle θ for the reflection of the reference ray:

$$\theta = \eta + \epsilon , \quad (16)$$

where

$$\epsilon = -\tfrac{1}{2}(\psi^2 + \delta_1^2)\tan\eta + \psi\delta_1/\cos\eta . \quad (17)$$

Rotation of the crystals through an angle $\Delta\eta$ about the monochromator axis causes the Bragg angle to change by $\Delta\eta + \Delta\epsilon(\eta, \psi, \delta)$. We call the angle η the *monochromator setting*.

Monochromator settings $0° < \eta < 90°$ are possible in principle, but in practice the geometry of the two-crystal device limits η to a smaller angular range. At the start of an experiment, an arbitrary stepping-motor unit number (conventionally, 200 000) is assigned to a monochromator setting

that corresponds to a first-order reflection in the region of the CuK edge. With respect to this reference setting, the stepping-motor units corresponding to other monochromator settings then are

$$\Delta(\text{motor units}) = 16\,000\Delta\eta\ , \tag{18}$$

where η is in degrees. Each angle η is now related to an angle θ, where $\theta = (\text{motor units})/16\,000$. The angle θ_0 corresponds to $\eta = 0$.

In order to find the absolute angles η, it is necessary to perform one absolute measurement which determines θ_0. This measurement must be repeated several times during each experiment, because orbit corrections after each filling of the electron storage ring can change the slope and position of the electron beam in the source region, affecting the x-ray angle of incidence on the monochromator crystals. We have observed ~3-eV energy changes of the diffracted photons between different fills, with the crystals left in a fixed position.

A precise absolute calibration procedure was developed to determine θ_0. The absorption edges of three elements (e.g., Zn, Cu, and Ni) are measured twice: with x rays that are Bragg reflected in first order and with x rays reflected in a higher order. For example, the first- and third-order reflections from the set of (111) Bragg planes can be used. One sharp, symmetric feature is identified in each spectrum (Fig. 3), and the angles θ_1 and θ_3 that correspond to this same feature in the first- and third-order spectra, respectively, are noted. Now the photon energy corresponding to one chosen symmetric feature is the same in the first-order spectrum and the third-order spectrum. According to Bragg's law, this energy is given by the two equations

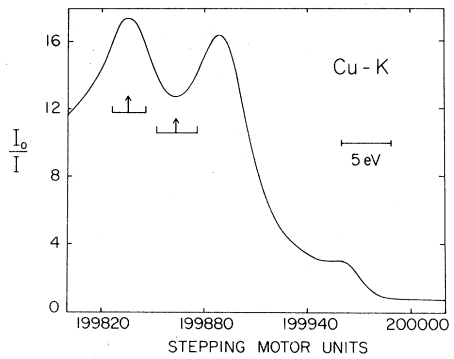

FIG. 3. Symmetric features in the Cu K-edge spectrum, indicated by arrows, used to calibrate the monochromator.

$$\frac{hc}{2d_1E} = \sin\left(\theta_1 - \theta_0 - \frac{\psi^2+\delta^2}{2}\tan(\theta_1-\theta_0) + \frac{\psi\delta}{\cos(\theta_1-\theta_0)}\right),$$

$$\frac{3hc}{2d_3E} = \sin\left(\theta_3 - \theta_0 - \frac{\psi^2+\delta^2}{2}\tan(\theta_3-\theta_0) + \frac{\psi\delta}{\cos(\theta_3-\theta_0)}\right). \tag{19}$$

By applying this procedure to three different spectral features, we obtain six equations with six unknowns. These equations can be solved for θ_0, ψ, and δ, and for the three energies of the three different features. If more than one feature in each of the absorption spectra is identified, an overdetermined set of equations is obtained. A computer routine that performs a least-squares analysis solves this set of equations.

Once ψ and δ are determined, only one absorption spectrum with one of the previously utilized features is needed to redetermine θ_0 after the storage ring has been refilled.

The bandwidth of the diffracted x-ray beam of a given energy is determined by the degree of collimation of the incident beam and by the Darwin function of the crystal.[21-23] In the arrangement employed in the present experiments, the geometrical factor dominates. Using the (220) reflecting planes of Si for 8-keV photons, e.g., the crystal window of the monochromator is ~0.02 mrad wide, full width at half maximum (FWHM),[24] while the geometrical window is ~0.1 mrad wide, FWHM. A monochromator setting η for the central ray then corresponds to a Bragg angle $\theta = \eta + \epsilon(\eta, \delta, \overline{\psi})$ for the centroid of the energy distribution of the diffracted x rays. The calibration procedure outlined above yields θ_0, $\overline{\psi}$, and δ corresponding to the central ray.

III. DATA ANALYSIS AND RESULTS

A. Theoretical model of absorption edges

The measured x-ray absorption spectra were analyzed with the aid of a theoretical model of absorption edges in the noble-gas samples. We consider only photoionization by the dominant electric-dipole transitions. The absorption cross section due to a particular one-electron transition from the nlj subshell of the ground state γ of a closed-shell atom to the $n'l'j'$ subshell of the level γ' can be written

$$\sigma_{\gamma\gamma'}(E) = A(\gamma,\gamma')E(R_{nl}^{n'l'})^2 \times \frac{\Gamma/2\pi}{[E-(E_{\gamma'}-E_{\gamma})]^2+(\Gamma/2)^2} . \quad (20)$$

Here, E denotes the photon energy, and $E_{\gamma'}-E_{\gamma}$ denotes the energy difference between the levels γ' and γ. The factor $A(\gamma,\gamma')$ contains all angular dependence, $R_{nl}^{n'l'}$ is the single-electron radial matrix element, and Γ is the width of the excited state γ'. The widths of all excited states associated with the same inner-shell vacancy are nearly equal, because the decay of the inner-shell vacancy is dominated by transitions determined by the distribution of the remaining core electrons.

To find the absorption cross section due to *all* one-electron transitions from the nlj state, we sum $\sigma_{\gamma\gamma'}(E)$ over all levels γ' that can be reached by electric-dipole transitions:

$$\sigma_{\gamma}(E) = \sum_{\gamma'} \sigma_{\gamma\gamma'}(E) . \quad (21)$$

The levels γ' are characterized by quantum numbers $n'l'j'$ if bound, and by $\epsilon l'j'$ if they lie in the continuum. We have

$$\sigma_{nlj}(E) = \sum_{n'l'j'} A(lj,l'j')E(R_{nl}^{n'l'})^2 \frac{\Gamma/2\pi}{[E-(E_{n'l'j'}-E_{nlj})]^2+(\Gamma/2)^2} + \sum_{l'j'} \int_0^{\infty} d\epsilon\, \rho_{l'j'}(\epsilon)A(lj,l'j')E(R_{nl}^{\epsilon l'})^2 \frac{\Gamma/2\pi}{[E(\epsilon-E_{nlj})]^2+(\Gamma/2)^2} , \quad (22)$$

where $\rho_{l'j'}(\epsilon)$ is the density of final states in which the ejected electron with angular-momentum quantum numbers $l'j'$ has kinetic energy in the interval $d\epsilon$ about ϵ.

Simplifying approximations can be made in Eq. (22) because we are only interested in the cross section for photon energies close to the binding energy of the nlj electrons, viz., for $E \cong |E_{nlj}| \pm 5$ eV. For these energies, the last Lorentz factor in Eq. (22) becomes very small unless $\epsilon < \sim 10$ eV. We therefore need to know the remainder of the integrand only for small ϵ. For closed-shell atoms, the radial integral $R_{nl}^{\epsilon l'}$ is a smooth, positive, monotonically decreasing function of ϵ.[25] We are hence led to approximate the second term in Eq. (22) by

$$\int_0^{\infty} d\epsilon \frac{a}{1+(E/b)^m} \frac{\Gamma/2\pi}{[E-(\epsilon-E_{nlj})]^2+(\Gamma/2)^2} , \quad (23)$$

where a, b, and m are constants. In fact, measured absorption curves are well fitted (Sec. III C) if we set $m=0$, i.e., if it is assumed that the function

$$\rho_{l'j'}(E)A(lj,l'j')E(R_{n'}^{\epsilon l'})^2$$

in Eq. (22) does not vary appreciably over the limited range of ϵ that contributes to the integral.[26] We furthermore shift the lower limit of the integral in Eq. (23) from 0 to $-\epsilon'$ (in practice, ~ -0.5 eV) to include with the continuum the highest bound states whose widths exceed their separation. The absorption cross section near the edge then becomes[27]

$$\sigma_{nlj}(E) \cong \sum_{n'l'j'} \frac{\Gamma/2\pi}{[E-(E_{n'l'j'}-E_{nlj})]^2+(\Gamma/2)^2} \quad \text{for } E_{n'l'j'} < \epsilon' + a\left(\frac{1}{2}+\frac{1}{\pi}\tan^{-1}\frac{2}{\Gamma}(E+E_{nlj}+\epsilon')\right) . \quad (24)$$

Over the limited energy scan (~ 10 eV) in an absorption-edge spectrum, the variation in the cross section $\sigma(E)$ can be ascribed entirely to the transitions that produce the edge. The incident x-ray beam ordinarily contains higher harmonics, consisting of more energetic photons diffracted in higher orders by the monochromator. For these photons, however, far in energy above the edges being studied, the absorption cross section varies approximately as E^{-3}, thus changing only by a fraction of one percent over a scan. Furthermore, the energy bandwidth of the incident beam is small compared with the width Γ of the discrete final states in the pertinent transitions. The shape of the absorption curve therefore is of the form

$$I(E)/I_0(E) = Ae^{-C\sigma_{nlj}(E)+B} , \quad (25)$$

where σ_{nlj} is given by Eq. (24), and the coefficients A, B, and C are constants.

To analyze an absorption-edge spectrum, the energies $E_{n'l'}$ and radial matrix elements $R_{nl}^{n'l'}$ were computed from Hartree-Slater wave functions[28] to serve as initial values in a computer fitting routine. A theoretical model of the absorption edge was calculated according to Eq. (25).

TABLE I. Transitions from the Ar 1s level.

Transition	Transition energy from absorption spectrum (eV)	Optical match [a] (eV)
$1s \rightarrow 4p$	3203.54	
$1s \rightarrow 5p$	3205.00	3204.99
$1s \rightarrow 6p$	3205.51	3205.52
$1s \rightarrow 7p$	3205.77	3205.77
$1s \rightarrow \infty$		3206.26

[a] Level energies obtained by adding optical level-energy differences from the $_{19}$K $I 3p^6(^1S)np$ series (Ref. 29) to the Ar $4p$-level energy derived from the absorption spectrum.

The transition energies and strengths, and the initial values of the constants A, B, and a, were then adjusted to attain a least-squares fit of model function and experimental data, minimizing

$$\chi^2 = \sum \left[\left(\frac{I_0(E)}{I(E)} \right)_{\text{model}} - \left(\frac{I_0(E)}{I(E)} \right)_{\text{data}} \right]^2 , \qquad (26)$$

where the sum is over all data points.

B. Linkage with the vacuum level

The least-squares fit of the theoretical-model spectrum to a measured absorption-edge spectrum yields experimental energy differences between the core level with which the edge is associated and four or five normally unoccupied bound states to which electric-dipole transitions from the core level can lead. The highest of these discrete bound states, discernible from the spectrum, is generally located ~0.5 eV below the vacuum level. The task remains to link the energy differences between core level and excited states to the vacuum level, so that absolute core-level binding energies can be deduced. This linkage with the vacuum level was established by matching the excited-state energies from the absorption spectrum of a noble gas with atomic number Z with the corresponding Rydberg-type level energies in the optical spectrum of the alkali element with atomic number $Z+1$.[29] It is assumed here that the photon-excited electron in a high-lying bound state about the singly ionized noble-gas core of element Z experiences a potential that is nearly identical with the potential seen by an excited valence electron in the $Z+1$ alkali atom. In fact, agreement between corresponding relative level energies in the absorption spectrum and in the associated optical spectrum was found to be always better than 0.1 eV (Sec. III C). The vacuum level could thus be associated with the limit of the pertinent optical spectral series.

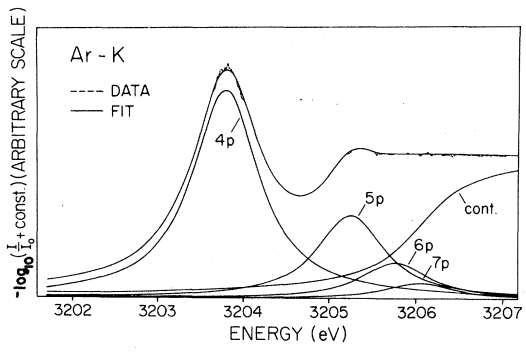

FIG. 4. Measured Ar absorption spectrum near the K edge and theoretical decomposition.

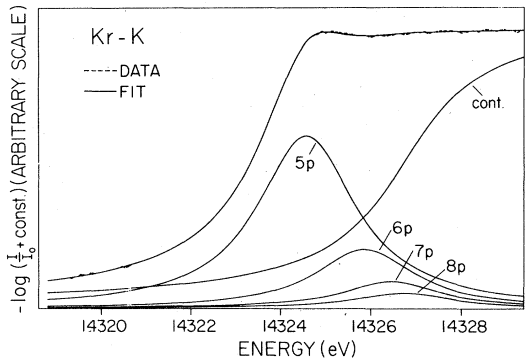

FIG. 5. Absorption spectrum of Kr near the K edge and fitted theoretical decomposition.

C. Results

Argon K edge. The theoretical model of the Ar K edge includes individual transitions $1s \rightarrow 4p$, $5p$, $6p$, $7p$ in the sum on the right-hand side of Eq. (24). Here as in all other cases, spin-orbit splitting is neglected, and we calculate average transition energies and the total transition probability for each pair of levels $n'p_{1/2}$ and $n'p_{3/2}$. In Table I, we list transition energies derived from the Ar 1s absorption spectrum (Fig. 4). We also show optical level differences from the $_{19}$K $I np\ ^2P^o$

TABLE II. Transitions from the Kr 1s level.

Transition	Transition energy from absorption spectrum (eV)	Optical match [a] (eV)
$1s \rightarrow 5p$	14 324.57	
$1s \rightarrow 6p$	14 325.86	14 325.94
$1s \rightarrow 7p$	14 326.45	14 326.44
$1s \rightarrow 8p$	14 326.72	14 326.69
$1s \rightarrow \infty$		14 327.17

[a] Level energies found by adding optical level-energy differences from the $_{37}$Rb $I 4p^6(^1S)np$ series (Ref. 29) to the Kr $5p$-level energy derived from the absorption spectrum.

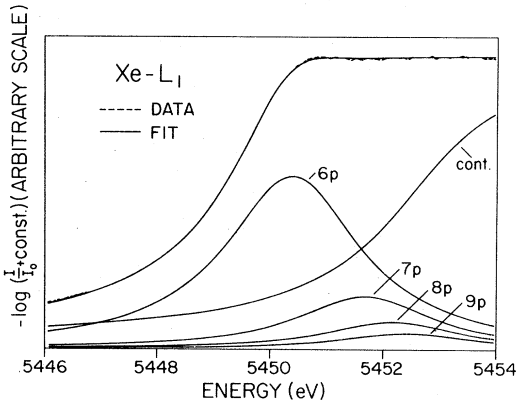

FIG. 6. Xenon L_1 absorption spectrum and theoretical fit.

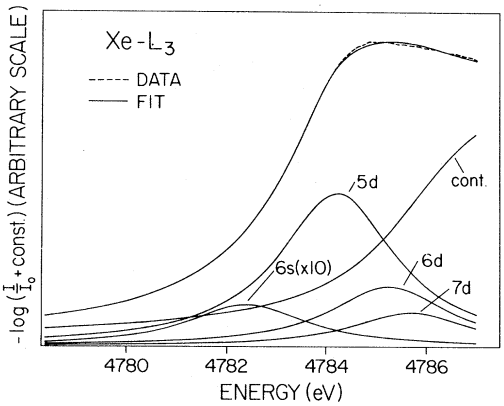

FIG. 8. Xenon L_3 absorption spectrum and theoretical fit.

series,[29] added to the present measured $1s \rightarrow 4p$ transition energy. The optical level energies are seen to match the energies derived from the absorption spectrum to better than 0.01 eV, so that the optical series limit can be used to establish the vacuum level at 3206.26 eV above the $1s$ level.

Krypton K edge. The $1s \rightarrow 5p$, $6p$, $7p$, and $8p$ discrete transitions were included in the analysis of the KrK edge (Fig. 5). The vacuum level is identified with the limit of the $_{37}$Rb I $np\ ^2P^o$ optical series[29] (Table II).

Xenon L edges. The Xe $2s$, $2p_{1/2}$, and $2p_{3/2}$ edge absorption spectra and their decompositions are illustrated in Figs. 6–8. The level energies are listed in Table III. In neutral ground-state Xe atoms, a $2p_{1/2}$ electron can undergo electric-dipole transitions to $n's$ ($n' \geq 6$) and $n'd_{3/2}$ ($n' \geq 5$) states. A $2p_{3/2}$ electron can reach these same states and, in addition, $n'd_{5/2}$ ($n' \geq 5$) states. The $n'd_{3/2}$ and $n'd_{5/2}$ levels are split by less than 0.05 eV, hence the average transition energy and total transition probability to each pair of levels was computed in the analysis of these spectra. The strength of $\rightarrow n'd$ transitions is more than ten times greater than that of $\rightarrow n's$ transitions. In modeling the Xe $2p$ absorption edges, we only find evidence for discrete transitions to the $6s$ and $5d$, $6d$, $7d$ levels.

Errors. Measured binding energies and their errors are summarized in Table IV. Errors are composed of uncertainties in the absolute energy scale, uncertainties in the least-squares fit of the model functions to absorption spectra, and the limits of consistency of the ≥ 3 independent measurements of each edge.

Uncertainties $\Delta\theta_B$ in the Bragg angle and Δd_n in

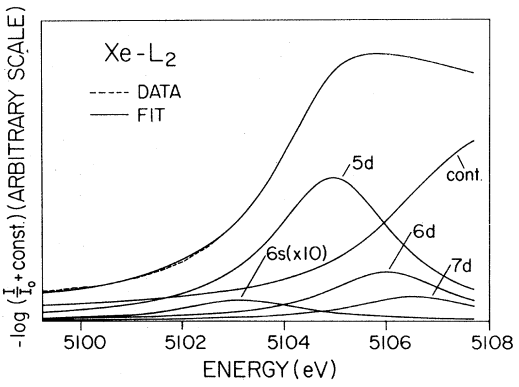

FIG. 7. Xenon L_2 absorption spectrum and theoretical fit.

TABLE III. Transitions from the Xe $2s$ and $2p$ levels.

Transition	Transition energy from absorption spectrum (eV)	Optical match [a] (eV)
$2s \rightarrow 6p$	5450.40	
$2s \rightarrow 7p$	5451.67	5451.68
$2s \rightarrow 8p$	5452.18	5452.16
$2s \rightarrow 9p$	5452.41	5452.40
$2s \rightarrow \infty$		5452.86
$2p_{1/2} \rightarrow 5d$	5104.88	
$2p_{1/2} \rightarrow 6d$	5105.93	5105.88
$2p_{1/2} \rightarrow 7d$	5106.45	5106.31
$2p_{1/2} \rightarrow 6s$	5103.09	5103.07
$2p_{1/2} \rightarrow \infty$		5106.98
$2p_{3/2} \rightarrow 5d$	4784.23	
$2p_{3/2} \rightarrow 6d$	4785.26	4785.23
$2p_{3/2} \rightarrow 7d$	4785.70	4785.65
$2p_{3/2} \rightarrow 6s$	4782.40	4782.42
$2p_{3/2} \rightarrow \infty$		4786.31

[a] Level energies obtained by adding optical level-energy differences from the $_{55}$Cs I $5p^6(^1S)nl$ series (Ref. 29) to the Xe $6p$- or $5d$-level energies, respectively, derived from the absorption spectra.

TABLE IV. Atomic electron binding energies (in eV). [a]

Level	Present	Experiment Bearden [b]	ESCA [c]	Theory [d]
Ar K	−3 206.3 (3)	−3 202.9 (3)	−3205.9 (5)	−3 205.39
Kr K	−14 327.2 (8)	−14 325.6 (8)		−14 325.78
Xe L_1	−5 452.9 (5)	−5 452.8 (4)	−5453.2 (4)	−5 458.70
Xe L_2	−5 107.0 (5)	−5 103.7 (4)	−5107.2 (4)	−5 106.73
Xe L_3	−4 786.3 (6)	−4 782.2 (4)	−4787.3 (4)	−4 786.54

[a] Numbers in parentheses indicate probable errors in the last significant figure.
[b] Reference 5.
[c] Reference 11.
[d] Reference 2.

the effective lattice spacing d_n [Eq. (2)] introduce an error ΔE in the absolute photon energy:

$$\Delta E = E \operatorname{cotan}\theta \Delta\theta_B + E(\Delta d_n/d_n). \tag{27}$$

We have

$$\Delta\theta_B = \Delta\theta_M + (\bar{\psi}\Delta\psi + \delta\Delta\delta)\tan\theta_M + (\cos\theta_M)^{-1}(\bar{\psi}\Delta\delta + \delta\Delta\bar{\psi}), \tag{28}$$

where θ_M is the monochromator setting for the central ray (Sec. II C). The uncertainty in the lattice constant[19,20] (Sec. II B) is

$$\Delta d_n = \Delta d\left(1 - \frac{4d^2}{n^2}\frac{\delta}{\lambda^2}\right) + \frac{4d^3}{n^2}\Delta\left(\frac{\delta}{\lambda^2}\right). \tag{29}$$

The computer fitting routine that finds the monochromator setting θ_M at the peak of a symmetric feature (Sec. II C) was designed also to compute the standard deviation for each parameter for the least-squares fit.[30] Two standard deviations (2σ) was used for the uncertainty.

The least-squares fitting program used to compute the transition energies was also written to compute the respective standard deviations. The error assigned to the fit of each edge is the greater of (i) the 2σ error from the least-squares fit of the model function to the absorption spectra or (ii) the maximum difference between any two results from at least three absorption spectra of any given edge, measured at different times.

D. Conclusions

In Table IV, the results of the present measurements are compared with x-ray energy levels of Bearden and Burr,[5] ESCA measurements of Siegbahn *et al.*,[11] and the theoretical Dirac-Hartree-Slater computations of Huang *et al.*[2] The absolute values of the level energies obtained in the present work lie systematically above those tabulated by Bearden and Burr.[5] Within limits of error, the present results agree with ESCA binding energies[11] where those exist, i.e., except for the Kr 1s state.

The theoretical self-consistent-field calculations[2] agree with measurements of the Xe L_2 and L_3 levels, within experimental errors. Slight discrepancies of the order of 1 eV exist for the Ar and Kr 1s levels; measurements indicate tighter binding than predicted by theory. These differences can be traced to the neglect of correlation in the Dirac-Hartree-Slater calculations of Ref. 2: A relativistic calculation[31] following Cowan's approach[32] shows that the correlation contribution to the 1s binding energies of both Ar and Kr is −1.08 eV, bringing theory into exact agreement with these measurements.

A striking discrepancy (~5 eV) is found for the Xe 2s state. This discrepancy is of a systematic nature, being common to elements throughout the periodic table.[2] It can well be surmised that the failure of the theoretical atomic model in the case of L_1 levels is also traceable to the independent-particle approximation inherent in the self-consistent-field approach. Many-body aspects, whether through electron-electron Coulomb correlation or through configuration interaction with bound and continuum states, may play an exceptionally pronounced role in the case of 2s vacancy states. These states lie close in energy to and have large wave-function overlap with $[2p][3d]nf$ or $[2p][3d]\epsilon f$ vacancy states that can be reached through virtual Coster-Kronig transitions. A related discrepancy is found with regard to the widths of 2s hole states in atoms in which transitions to these $[2p][3d]nf, \epsilon f$ states are energetically possible, i.e., for $Z < 50$ and $Z > 75$: Independent-particle calculations invariably overestimate these widths by as much as a factor of 3.[33,34] The discrepancy is not resolved by taking account of relativity, exchange between continuum and bound-state electrons in the decay through radiationless transitions, and imperfect wave-function overlap between initial- and final-state atoms.[35] In an analogous outer (M)-shell problem, however, a

many-body approach has been shown to resolve the difficulty.[36] For inner-shell vacancy states in any but the lightest atoms, many-body calculations have not yet been performed.

ACKNOWLEDGMENTS

We are grateful for the expert technical assistance of Bob Filippi. This work was supported in part by the U.S. Army Research Office, under Grant No. DAAG29-78-G-0010, and by the Air Force Office of Scientific Research (Grant No. 79-0026). Some of the materials incorporated in this work were developed at the Stanford Synchrotron Radiation Laboratory which is supported by the National Science Foundation (under Contract No. DMR77-27489), in cooperation with Stanford Linear Accelerator Center and the Department of Energy.

---

*Present address: Department of Physics, University of Tennessee, Knoxville, Tennessee 37916.
†Present address: Oak Ridge National Laboratory, P. O. Box X, Oak Ridge, Tennessee 37830.
‡Present address: Laboratório de Física da Universidade de Lisboa, Rua da Escola Politécnica, Lisboa-2, Portugal.

[1]R. D. Deslattes, L. Jacobs, E. G. Kessler, Jr., and W. Schwitz, Phys. Lett. 71A, 411 (1979).
[2]K.-N. Huang, M. Aoyagi, M. H. Chen, B. Crasemann, and H. Mark, At. Data Nucl. Data Tables 18, 243 (1976).
[3]J. P. Desclaux, At. Data Nucl. Data Tables 12, 311 (1973).
[4]K. T. Cheng and W. R. Johnson, Phys. Rev. A 14, 1943 (1976).
[5]J. A. Bearden and A. F. Burr, Rev. Mod. Phys. 39, 125 (1967).
[6]W. Lotz, J. Opt. Soc. Am. 57, 873 (1967); 58, 236 (1968); 58, 915 (1968); 60, 209 (1970).
[7]K. Siegbahn, C. Nordling, A. Fahlman, R. Nordberg, K. Hamrin, J. Hedman, G. Johansson, T. Bergmark, S. Karlsson, I. Lindgren, and B. Lindberg, Nova Acta Regiae Soc. Sci. Ups. 20 (1967).
[8]L. Ley, S. P. Kowalczyk, F. R. McFeely, R. A. Pollak, and D. A. Shirley, Phys. Rev. B 8, 2393 (1973).
[9]D. A. Shirley, R. L. Martin, S. P. Kowalczyk, F. R. McFeely, and L. Ley, Phys. Rev. B 15, 544 (1977).
[10]R. E. Watson, M. L. Perlman, and J. Herbst, Phys. Rev. B 13, 2358 (1976).
[11]K. Siegbahn, C. Nordling, G. Johansson, J. Hedman, P. F. Hedén, K. Hamrin, U. Gelius, T. Bergmark, L. O. Werme, R. Manne, and Y. Baer, *ESCA Applied to Free Molecules* (North-Holland, Amsterdam, 1971).
[12]E. G. Kessler, Jr., R. D. Deslattes, and A. Henins, Phys. Rev. A 19, 215 (1979).
[13]M. O. Krause and C. W. Nestor, Jr., Phys. Scr. 16, 285 (1977).
[14]R. D. Deslattes, Jpn. J. Appl. Phys. 17, Suppl. 17-2, 1 (1979).
[15]H. Winick and A. Bienenstock, Annu. Rev. Nucl. Part. Sci. 28, 33 (1978).
[16]I. Lindau and H. Winick, Stanford Synchrotron Radiation Laboratory Report No. SSRP 76/12, 1976 (unpublished).
[17]B. M. Kincaid, Stanford Synchrotron Radiation Laboratory Report No. SSRP 75/03, 1975 (unpublished).
[18]I. Henins and J. A. Bearden, Phys. Rev. 135, A890 (1964).
[19]R. D. Deslattes and A. Henins, Phys. Rev. Lett. 31, 972 (1973); R. D. Deslattes, A. Henins, R. M. Schoonover, C. L. Carroll, and H. A. Bowman, *ibid.* 36, 898 (1976).
[20]E. G. Kessler, Jr., R. D. Deslattes, A. Henins, and W. C. Sauder, Phys. Rev. Lett. 40, 171 (1978).
[21]C. G. Darwin, Philos. Mag. 27, 315 (1914); 27, 675 (1914).
[22]J. A. Prins, Z. Phys. 63, 477 (1930).
[23]B. W. Batterman and H. Cole, Rev. Mod. Phys. 36, 681 (1964).
[24]K. Kohra, M. Ando, T. Matsushita, and H. Hashizume, in *Synchrotron Radiation Instrumentation and New Developments*, edited by F. Wuilleumier and Y. Farge (North-Holland, Amsterdam, 1978), p. 161.
[25]U. Fano and J. W. Cooper, Rev. Mod. Phys. 40, 441 (1968).
[26]T. Watanabe, Phys. Rev. 137, A1380 (1965).
[27]M. Breinig, Ph. D. thesis, University of Oregon, 1979 (unpublished).
[28]F. Herman and S. Skillman, *Atomic Structure Calculations* (Prentice-Hall, Englewood Cliffs, 1963).
[29]C. E. Moore, *Atomic Energy Levels*, National Stand. Ref. Data. Ser. (Nat. Bureau of Standards Cir. 467, Washington D. C., Vol. I, 1949, Vol. II, 1952, and Vol. III, 1958).
[30]P. R. Bevington, *Data Reduction and Error Analysis for the Physical Sciences* (McGraw-Hill, New York, 1969), Eq. (11-30).
[31]M. H. Chen (private communication).
[32]R. D. Cowan, Phys. Rev. 163, 54 (1967).
[33]M. O. Krause and J. H. Oliver, J. Phys. Chem. Ref. Data 8, 329 (1979).
[34]M. H. Chen, B. Crasemann, M. Aoyagi, and H. Mark, Phys. Rev. A 15, 2312 (1977).
[35]M. H. Chen, B. Crasemann, M. Aoyagi, and H. Mark, Phys. Rev. A 18, 802 (1978).
[36]M. Ohno and G. Wendin, Solid State Commun. 24, 75 (1977).